Air Force Institute of Technology

# AFIT Scholar

4-22-2015

# Interstitial Silicon Ions in Rutile TiO$_2$ Crystals

Eric M. Golden

Nancy C. Giles
*Air Force Institute of Technology*

Shan Yang
*Jackson State University*

Larry E. Halliburton
*West Virginia University*

## Recommended Citation

Golden, E. M., Giles, N. C., Yang, S., & Halliburton, L. E. (2015). Interstitial silicon ions in rutile TiO2 crystals. Physical Review B (Condensed Matter and Materials Physics), 91(13), 134110. https://doi.org/10.1103/PhysRevB.91.134110

# Interstitial silicon ions in rutile TiO₂ crystals

E. M. Golden,[1] N. C. Giles,[1] Shan Yang (杨山),[2] and L. E. Halliburton[3,*]

[1]*Department of Engineering Physics, Air Force Institute of Technology, Wright-Patterson Air Force Base, Ohio 45433, USA*
[2]*Department of Physics, Atmospheric Sciences, and Geoscience, Jackson State University, Jackson, Mississippi 39217, USA*
[3]*Department of Physics and Astronomy, West Virginia University, Morgantown, West Virginia 26506, USA*

Electron paramagnetic resonance (EPR) is used to identify a new and unique photoactive silicon-related point defect in single crystals of rutile TiO₂. The importance of this defect lies in its assignment to interstitial silicon ions and the unexpected establishment of silicon impurities as a major hole trap in TiO₂. Principal $g$ values of this new $S = 1/2$ center are 1.9159, 1.9377, and 1.9668 with principal axes along the [$\bar{1}$10], [001], and [110] directions, respectively. Hyperfine structure in the EPR spectrum shows the unpaired spin interacting equally with two Ti nuclei and unequally with two Si nuclei. These silicon ions are present in the TiO₂ crystals as unintentional impurities. Principal values for the larger of the two Si hyperfine interactions are 91.4, 95.4, and 316.4 MHz with principal axes also along the [$\bar{1}$10], [001], and [110] directions. The model for the defect consists of two adjacent Si ions, one at a tetrahedral interstitial site and the other occupying a Ti site. Together, they form a neutral nonparamagnetic $[Si_{int} - Si_{Ti}]^0$ complex. When a crystal is illuminated below 40 K with 442-nm laser light, holes are trapped by these silicon complexes and form paramagnetic $[Si_{int} - Si_{Ti}]^+$ defects, while electrons are trapped at oxygen vacancies. Thermal anneal results show that the $[Si_{int} - Si_{Ti}]^+$ EPR signal disappears in two steps, coinciding with the release of electrons from neutral oxygen vacancies and singly ionized oxygen vacancies. These released electrons recombine with the holes trapped at the silicon complexes.

## I. INTRODUCTION

Electron and hole traps occurring in the bulk or near the surface of TiO₂ crystals are of considerable interest because of the critical role they play in photocatalytic mechanisms in this widely studied material [1,2]. Although trapped electrons, primarily in the form of Ti³⁺ ions, have been well characterized in rutile TiO₂ crystals [3–16], little is presently known about the defects that trap holes during photoexcitation. Intrinsic self-trapped holes, i.e., holes localized on an oxygen ion with no nearby defect, have been identified in these crystals [17], but they are only stable at low temperatures (<10 K). Nitrogen ions, substituting for oxygen ions, are acceptors in TiO₂ and have been investigated both computationally and experimentally in rutile and anatase nanocrystals [18,19]. Also, the possibility of a titanium vacancy acting as a hole trap in TiO₂ has been considered in computational studies [20,21], but detailed experiments describing this defect have not been reported.

In the present paper, we describe results from an electron paramagnetic resonance (EPR) study showing that an interstitial silicon ion, when bound to a second silicon ion substituting for a titanium ion, can serve as a hole trap in bulk rutile TiO₂ crystals. Significant concentrations of these silicon complexes are unintentionally present in many commercially available TiO₂ crystals. Two charge states are possible for these complexes, neutral and nonparamagnetic $[Si_{int} - Si_{Ti}]^0$ or positive and paramagnetic $[Si_{int} - Si_{Ti}]^+$. In a crystal with a sufficiently low Fermi level, the EPR spectrum from the $[Si_{int} - Si_{Ti}]^+$ defect is observed without illumination. When the Fermi level is high, the EPR spectrum must be photoinduced at low temperatures using near-band-gap

laser light. Most as-grown undoped rutile bulk TiO₂ crystals are in this latter category and require light to produce the paramagnetic charge state of the defect. Resolved hyperfine interactions with two inequivalent silicon nuclei and two equivalent titanium nuclei are present in the EPR spectrum. Principal values and principal-axis directions of the $g$ matrix and the two ²⁹Si hyperfine matrices are obtained from the angular dependence of the spectrum. These sets of parameters are used to construct a detailed model of the silicon-related defect that places the interstitial silicon ion at a tetrahedral position. A pulsed thermal anneal conducted between 20 and 50 K after a crystal was exposed to laser light provides verification that the $[Si_{int} - Si_{Ti}]^+$ center represents a trapped hole.

## II. EXPERIMENTAL DETAILS

The undoped rutile TiO₂ crystal used in the present investigation was grown at CrysTec (Berlin, Germany) by the Verneuil method. In addition to silicon impurities, EPR showed that this crystal contains trace amounts of chromium, copper, iron, and vanadium. Doubly ionized oxygen vacancies were also present in the as-grown crystal and served as charge compensators for trivalent metal ions substituting for Ti⁴⁺ ions. Two samples suitable for EPR experiments, each $3 \times 3 \times 2$ mm³, were cut from the larger $c$ plate provided by CrysTec. One sample was left in its as-grown state (and is referred to in this paper as sample A). Lithium was diffused into the other sample (referred to herein as sample B). The lithium diffusion was performed by immersing the crystal in lithium hydroxide powder and then holding it for 6 h at 450 °C while surrounded by static air.

The space group for rutile TiO₂ is $P4_2/mnm(D_{4h}^{14})$ with lattice constants of $a = 4.5937$ Å, $c = 2.9587$ Å, and $u = 0.30478$ [22,23]. In this tetragonal crystal, titanium ions have
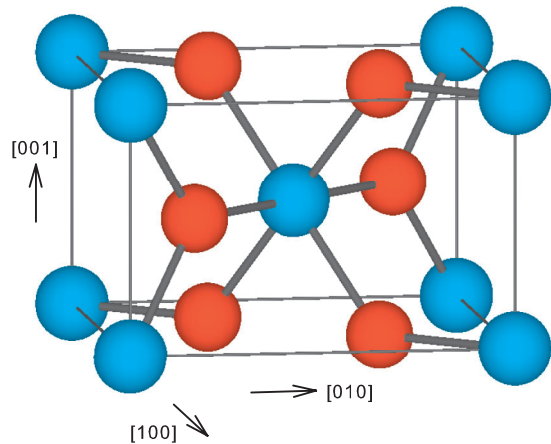
*Corresponding author: larry.halliburton@mail.wvu.edu

FIG. 1. (Color online) Schematic of the rutile $TiO_2$ crystal structure, showing one of the two equivalent $TiO_6$ octahedra and its eight neighboring Ti neighbors.

six oxygen neighbors and oxygen ions have three titanium neighbors. Slightly distorted $TiO_6$ octahedra are alternately elongated in the [110] and [$\bar{1}$10] directions (these equivalent octahedra are related by a 90° rotation about the [001] direction). Figure 1 shows one of the two $TiO_6$ units and its eight nearest-neighbor Ti ions. The six oxygen ions within the octahedron separate into a set of four equatorial oxygens and a set of two apical oxygens. At room temperature, the four equatorial oxygen ions are 1.9485 Å from the central titanium ion, and the two apical oxygen ions are 1.9800 Å from the titanium ion [22].

The EPR spectra were taken with a Bruker EMX spectrometer operating near 9.5 GHz. A cylindrical $TE_{011}$ microwave cavity was used. The sample temperature was controlled with an Oxford helium-gas-flow system, and the static magnetic field was measured with a proton NMR teslameter. A Cr-doped MgO crystal was used to correct for small differences in magnetic-field strength between the position of the sample in the microwave cavity and the tip of the teslameter probe ($Cr^{3+}$ ions in MgO have a known isotropic $g$ value of 1.9800). Samples were illuminated at low temperatures in the microwave cavity with 442-nm light from a He-Cd laser.

## III. RESULTS

### A. Silicon-related EPR spectrum

Figure 2 shows the silicon-related EPR spectrum obtained from sample A, the as-grown nominally undoped $TiO_2$ crystal. Throughout Sec. III, the defect being studied is referred to as silicon related. Then, in Sec. IV, a detailed model is established, and the defect is given the more precise label $[Si_{int} - Si_{Ti}]$. The spectrum in Fig. 2 was taken at 40 K with the magnetic field along the [001] direction and with 442-nm laser light incident on the sample. To minimize the effects of saturation, the microwave power was low ($\sim 6.3\,\mu$W). This $S = 1/2$ EPR signal in Fig. 2 was observed in the as-grown sample before illumination, but exposure to the laser light while the sample was at low temperature significantly increased the intensity of the signal. In an earlier study, Yang *et al.* [10] reported the spectrum shown in Fig. 2 and tentatively
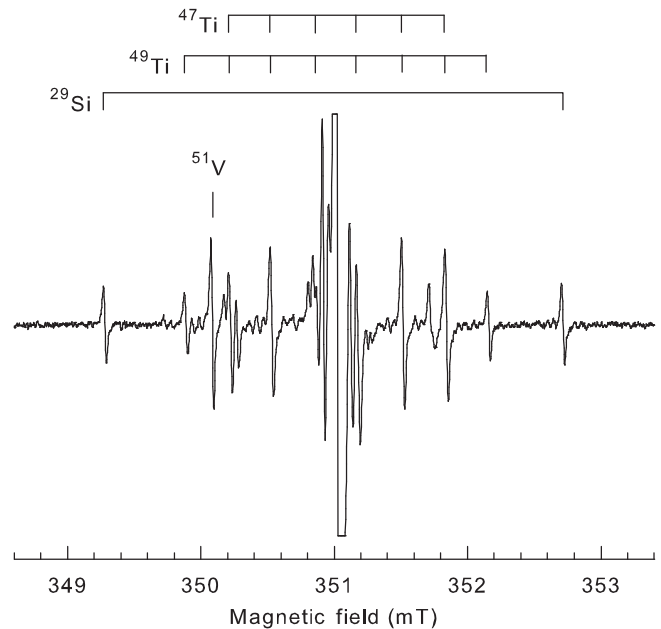


FIG. 2. EPR spectrum of the $[Si_{int} - Si_{Ti}]^+$ defect in an as-grown oxidized rutile $TiO_2$ crystal. The sample temperature was 40 K, the magnetic field was along the [001] direction, and the microwave frequency was 9.520 GHz. The sample was exposed to 442-nm laser light while acquiring the spectrum.

assigned it to a trapped-electron center (i.e., a $Ti^{3+}$ ion adjacent to a substitutional $Si^{4+}$ ion located at a $Ti^{4+}$ site). Our present investigation shows that the early assignment was incomplete.

The EPR spectrum in Fig. 2 has a large central line symmetrically surrounded by sets of lower intensity hyperfine lines. The majority of these hyperfine lines are due to interactions of the unpaired spin with $^{47}$Ti and $^{49}$Ti nuclei ($^{47}$Ti has $I = 5/2$ and is 7.4% abundant whereas $^{49}$Ti has $I = 7/2$ and is 5.4% abundant). As indicated by the stick diagrams above the spectrum in Fig. 2, there is a set of six hyperfine lines for $^{47}$Ti nuclei and a set of eight lines for $^{49}$Ti nuclei. The set of six lines overlaps the inner six lines of the set of eight lines because the magnetic moments of the two isotopes are similar. Measurements of the intensities of the $^{47}$Ti and $^{49}$Ti hyperfine lines relative to the central line show that two titanium ions are contributing to the hyperfine pattern (i.e., there are two titanium neighbors participating equally in the defect). This is demonstrated by a comparison of the intensity of the highest field $^{49}$Ti line (at 352.1 mT) to the intensity of the central $I = 0$ line (at 351.0 mT). The measured intensity ratio of these two lines in Fig. 2 is 64.1, and the predicted ratios are 139.9 for one titanium neighbor and 69.9 for two titanium neighbors. The experimental ratio strongly supports the presence of two titanium neighbors that contribute equally to the hyperfine pattern. Lack of exact agreement with the predicted ratio for two equal titanium neighbors is most likely due to slightly different microwave power saturation behaviors of the central $I = 0$ line and the $^{49}$Ti hyperfine line.

In addition to the titanium hyperfine lines, there is a widely separated pair of lines located near 349.3 and 352.7 mT in Fig. 2 that is due to a hyperfine interaction with a $^{29}$Si nucleus ($^{29}$Si has $I = 1/2$ and is 4.67% abundant). Also, there are

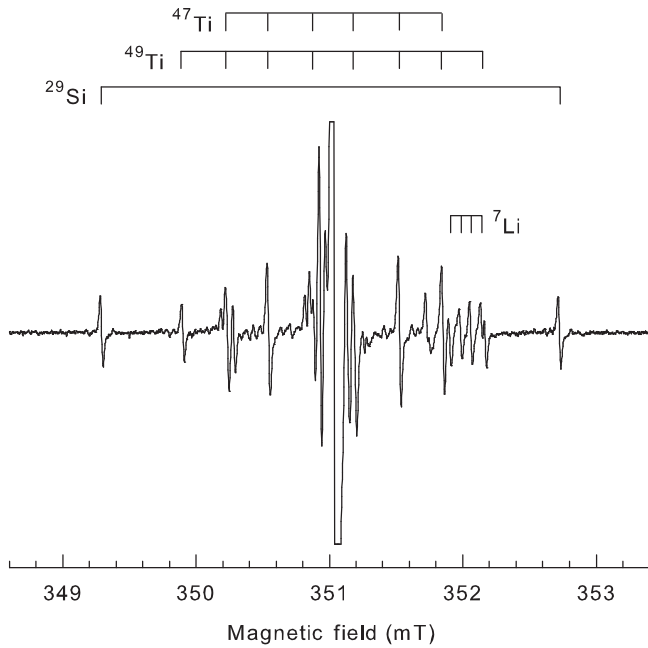FIG. 3. EPR spectrum of the $[Si_{int} - Si_{Ti}]^+$ defect in a rutile TiO₂ crystal diffused with lithium. The sample temperature was 40 K, the magnetic field was along the [001] direction, and the microwave frequency was 9.520 GHz. There was no laser light on the sample.



FIG. 4. EPR spectrum of the $[Si_{int} - Si_{Ti}]^+$ defect in a rutile TiO₂ crystal diffused with lithium. The temperature was 40 K, the field was along the [100] direction, and the microwave frequency was 9.520 GHz. There was no laser light on the sample.

slightly resolved hyperfine lines located very close to the central $I = 0$ line in Fig. 2 (within 0.3 mT) that are due to more distant $^{47,49}$Ti nuclei and to a second weakly interacting $^{29}$Si nucleus. An unrelated photoinduced line at 350.1 mT is one of the set of eight widely split hyperfine lines arising from trace concentrations of $V^{4+}$ $(3d^1)$ ions substituting for $Ti^{4+}$ ions ($^{51}$V nuclei have $I = 7/2$ and are 100% abundant) [24].

Next, consider sample B, the lithium-diffused TiO₂ crystal. As can be seen in Fig. 3, the silicon-related defect is present in this sample. These data in Fig. 3 were taken at 40 K with the magnetic field along the [001] direction and thus can be directly compared to the spectrum in Fig. 2. The only differences in the spectra in Figs. 2 and 3 are the presence of the $V^{4+}$ signal near 350.1 mT in Fig. 2 and the presence of a four-line Li-related signal [12] near 352.0 mT in Fig. 3. Laser light was not needed to produce the silicon-related signal in sample B (i.e., the spectrum in Fig. 3 was taken after cooling to 40 K in the dark). Subsequent exposure to 442-nm laser light at low temperatures did not increase the intensity of the spectrum. This behavior suggests that the Fermi level has moved lower in sample B, compared to sample A. This is not unexpected since the lithium diffusion occurred while the sample was held at high temperature in air, an oxidizing atmosphere, and surrounded by oxygen in the form of the hydroxide powder.

Figure 4 shows the silicon-related EPR spectrum in sample B when the magnetic field is along the [100] direction. There is again a large central line surrounded by less intense hyperfine lines. The hyperfine lines from the $^{47}$Ti and $^{49}$Ti nuclei, although present, are not easily separated into a six-line set and an eight-line set for this direction of magnetic field because of interference from forbidden transitions caused by significant nuclear-electric-quadrupole interactions. Weak
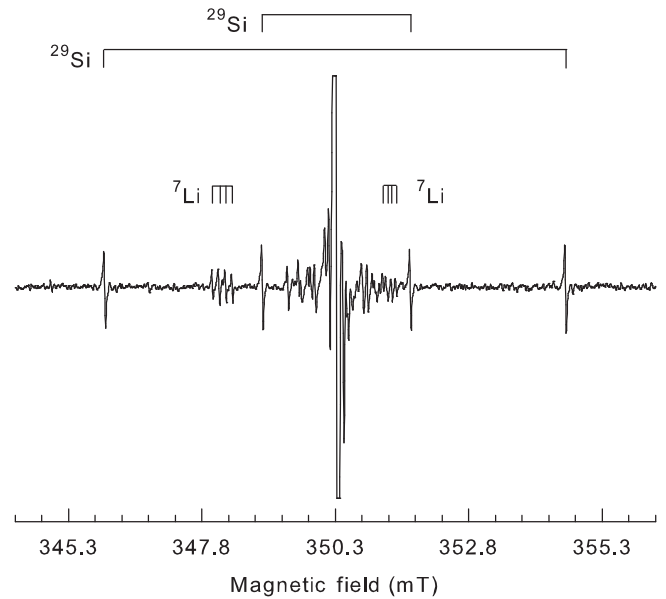
four-line lithium-related signals are present near 348.2 and 351.3 mT. The [100] EPR spectrum in Fig. 4 shows widely split pairs of lines due to the unequal hyperfine interactions with two $^{29}$Si nuclei. Hyperfine lines from one $^{29}$Si nucleus are located at 346.0 and 354.6 mT, and hyperfine lines from a second $^{29}$Si nucleus are located at 348.9 and 351.7 mT. Measurement yields 37.4 for the intensity ratio of the highest field $^{29}$Si line (at 354.6 mT) and the central $I = 0$ line (at 350.3 mT). This experimental value is close to the predicted intensity ratio of 40.7 for one participating nucleus, thus verifying that this outer pair of $^{29}$Si lines in Fig. 4 arises from one silicon nucleus. A similar argument shows that the inner pair of $^{29}$Si lines in Fig. 4 is also produced by one silicon nucleus. Together, the EPR spectra in Figs. 2–4 establish that the responsible point defect has significant hyperfine interactions with two silicon nuclei and two titanium nuclei.

### B. Spin-Hamiltonian parameters

The angular dependence of the silicon-related EPR spectrum is shown in Fig. 5. These data were obtained at 40 K from sample B (laser light was not incident on the crystal before or during this angular study). Results for the central $I = 0$ line and the two pairs of $^{29}$Si lines are plotted in Fig. 5 for rotation of the magnetic field in three high-symmetry planes. A detailed angular dependence of the $^{47}$Ti and $^{49}$Ti hyperfine lines was not acquired because of the lack of resolution caused by overlapping lines and the presence of nuclear-electric-quadrupole-induced forbidden lines. These $^{47,49}$Ti lines are clearly resolved only along the [001] direction. Sample B was used for the angular-dependent study because light was not required to produce the silicon-related spectra. This prevented interference from photoinduced oxygen-vacancy EPR signals [15,16].
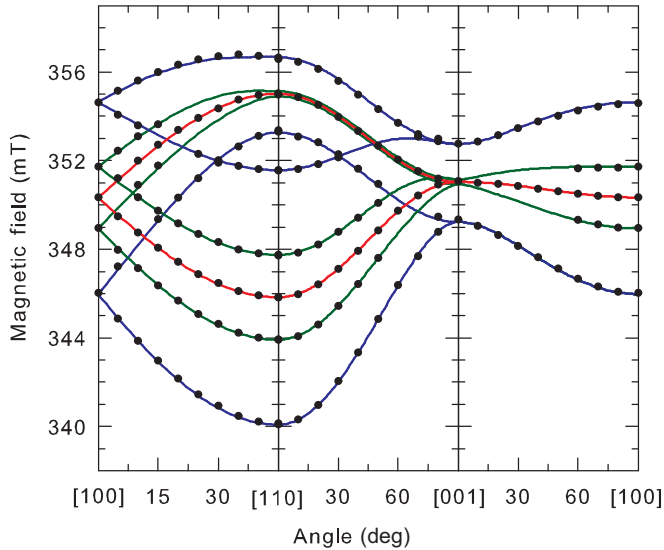
FIG. 5. (Color online) EPR angular dependence (in three high-symmetry planes) of the $[Si_{int} - Si_{Ti}]^+$ defect. Red lines represent defects with no $^{29}Si$ nuclei, whereas the green and blue lines represent the two separate $^{29}Si$ nuclei. Discrete points are experimental results. Solid curves were calculated using the parameters in Table I and a microwave frequency of 9.520 GHz.

TABLE I. Spin-Hamiltonian parameters for the $[Si_{int} - Si_{Ti}]^+$ center in rutile $TiO_2$ crystals. Units for the hyperfine parameters are MHz. Uncertainties are estimated to be $\pm 0.0002$ for the $g$ values and $\pm 1.0$ MHz for the $A$ values. Relative signs of the hyperfine parameters were not determined.

| | Principal value | Principal-axis direction |
|---|---|---|
| | *g* matrix | |
| $g_1$ | 1.9159 | $[\bar{1}10]$ |
| $g_2$ | 1.9377 | $[001]$ |
| $g_3$ | 1.9668 | $[110]$ |
| | $A$-hyperfine matrix for smaller $^{29}Si$ interaction | |
| $A_1$ | 0.3 | $[\bar{1}10]$ |
| $A_2$ | 0.8 | $[001]$ |
| $A_3$ | 105.3 | $[110]$ |
| | $A$-hyperfine matrix for larger $^{29}Si$ interaction | |
| $A_1$ | 91.4 | $[\bar{1}10]$ |
| $A_2$ | 95.4 | $[001]$ |
| $A_3$ | 316.4 | $[110]$ |

In Fig. 5, the silicon-related EPR spectrum separates into two branches when the magnetic field is rotated from [100] to [110] and from [110] to [001]. In contrast, a splitting does not occur when the field is rotated from [001] to [100]. For an arbitrary direction of magnetic field (well away from these three planes), the maximum number of primary $I = 0$ lines remains two. These observations demonstrate that there are two magnetically inequivalent, but crystallographically equivalent, orientations of the silicon-related defect. By focusing on the angular dependence associated with the $g$ matrix (i.e., the red lines in Fig. 5), the principal axes of this matrix can be determined. Along the [110] direction, one branch of these $I = 0$ lines has a high-field turning point, and the other branch has a low-field turning point. This establishes that the $g$ matrix has two of its principal axes along 110 directions, and thus the third principal axis must be along the [001] direction. The same argument is made for the directions of the principal axes of the hyperfine matrix representing the $^{29}Si$ lines having the larger interaction (i.e., the blue lines in Fig. 5). When the field is along the [110] direction, the observed separation of these hyperfine lines reaches a maximum (11.5 mT) for the lower-field branch and a minimum (3.3 mT) for the higher-field branch. This establishes that the larger $^{29}Si$ hyperfine interaction matrix has two of its principal axes along the 110 directions. Again, to preserve an orthogonal coordinate set, the third principal axis must be along the [001] direction.

The $^{29}Si$ lines representing the smaller hyperfine interaction (i.e., the green lines in Fig. 5) also have a maximum separation (3.8 mT) in the lower branch when the field is along the [110] direction. This establishes that this smaller $^{29}Si$ hyperfine matrix has at least one principal axis along a 110 direction. The corresponding upper branch has a very small separation of its two hyperfine lines when the field is along the [110]

direction (the actual separation is not measured because these lines are overlapped by hyperfine lines from $^{47,49}Ti$ nuclei). This separation within the upper branch continues to be small as the field is rotated from [110] to [001]. Despite these reduced separations, the other two principal axes of the hyperfine matrix describing this second $^{29}Si$ interaction can be determined from the data in Fig. 5. Splitting into two branches does not occur for the smaller $^{29}Si$ interaction when the magnetic field is rotated from [001] to [100]. This provides sufficient evidence to establish that one of the remaining principal axes of this hyperfine matrix must be along another of the equivalent 110 directions and that the third principal axis must be along the [001] direction.

The following spin Hamiltonian can be used to describe the $S = 1/2$ silicon-related EPR spectrum in the rutile $TiO_2$ crystals,

$$H = \beta \mathbf{S} \cdot \mathbf{g} \cdot \mathbf{B} + \mathbf{I} \cdot \mathbf{A} \cdot \mathbf{S} - g_n \beta_n \mathbf{I} \cdot \mathbf{B}. \qquad (1)$$

This Hamiltonian contains electron Zeeman, hyperfine, and nuclear Zeeman terms and describes an interaction of the unpaired spin with one magnetic nucleus. Because of the low abundance of the $^{29}Si$ nuclei (4.67%), most of the defects contributing to the EPR spectrum have only one of the two silicon sites occupied by a magnetic nucleus, and thus there is no need to consider a spin Hamiltonian containing two $^{29}Si$ hyperfine interactions. Having already established the directions of the principal axes of the $g$ matrix, the principal values of this matrix were obtained by a least-squares fitting using the angular dependence of the $I = 0$ lines in Fig. 5 (i.e., the red lines) and the first term in Eq. (1). The results for the $g$ matrix are listed in Table I. Next, the complete spin Hamiltonian in Eq. (1) was used to separately determine the principal values of the $^{29}Si$ hyperfine matrices (with the $g$ matrix now fixed at its final values). As was the case for the $g$ matrix, the directions of the principal axes for both $^{29}Si$ matrices were already known. Final values of each set of principal values were then determined by independently fitting the $^{29}Si$ angular dependence data in Fig. 5 (the blue and the green sets). The results are listed in Table I. The solid curves
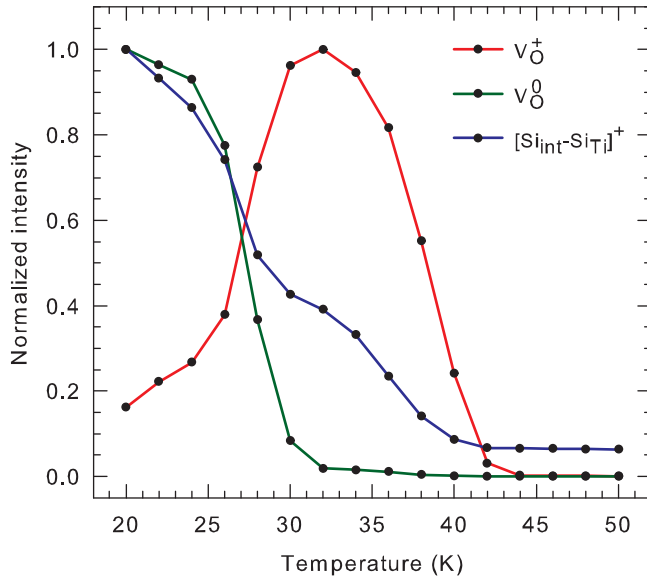
FIG. 6. (Color online) EPR isochronal pulsed anneal results. The crystal was initially illuminated at 20 K and then kept in the dark for the remainder of the experiment. The green curve is the neutral oxygen vacancy, the red curve is the singly ionized oxygen vacancy, and the blue curve is the [Si$_{int}$ − Si$_{Ti}$]$^+$ defect.

in Fig. 5 were computer generated using these principal values in Table I.

### C. Evidence that the silicon-related center is a hole trap

An isochronal annealing experiment provided information about the thermal stability of the paramagnetic charge state of the silicon-related defect in sample A, the as-grown crystal. Although the EPR spectrum representing this defect is present without light in this crystal, its intensity is greatly enhanced by an exposure at 20 K to 442-nm laser light. After an illumination at 20 K, signals from neutral oxygen vacancies and singly ionized oxygen vacancies along with the signal from the silicon-related center are present in the EPR spectrum taken at 20 K with the magnetic field along the [001] direction. Once this spectrum was acquired, the laser light was removed, and no further illumination occurred during the annealing experiment. With the crystal remaining in the microwave cavity, its temperature was raised to 22 K and held there for 30 s. The crystal was then returned to 20 K and the EPR spectrum was taken again. This incremental annealing process was repeated in 2 K steps with 30-s holding times at each elevated temperature. Following each anneal step, the EPR spectrum was recorded at the 20-K monitoring temperature. Figure 6 shows the normalized results of these thermal anneals.

In Fig. 6, neutral oxygen vacancies (V$_O^0$), each with two trapped electrons, rapidly decay between 24 and 30 K. The singly ionized oxygen vacancies (V$_O^+$) grow as the neutral oxygen vacancies are thermally destroyed. This is expected since V$_O^0$ centers become V$_O^+$ centers when one electron is removed. Between 32 and 42 K, the V$_O^+$ centers are destroyed as the second electron is thermally removed. The silicon-related EPR spectrum disappears in two stages with each stage corresponding to a temperature region where oxygen vacancies

release electrons. The first step, between 22 and 30 K, coincides with the release of electrons from the neutral oxygen vacancies. The second step, between 32 and 42 K, coincides with the release of electrons from the singly ionized oxygen vacancies. These thermally released electrons annihilate holes that are trapped at the silicon-related defect.

## IV. INTERSTITIAL SILICON MODEL

Significant amounts of silicon impurities are often present in bulk rutile TiO$_2$ crystals [25,26]. Thus, it is not surprising to find a photoinduced paramagnetic defect associated with silicon in this material. The hyperfine results show that two unequal silicon ions and two equal titanium ions are major features of the observed defect. Also, the measured $g$ shifts are negative (i.e., the principal $g$ values are less than 2.0), and the principal-axis directions of the $g$ matrix and the $^{29}$Si hyperfine matrices are along high-symmetry directions, specifically [110] and [001] directions. In this section, a model of the silicon-related defect is constructed that satisfies these constraints.

For silicon ions in TiO$_2$, the expectation would be for a Si$^{4+}$ ion to replace a Ti$^{4+}$ ion. The ionic radius of a Si$^{4+}$ ion is considerably smaller than the radius of a Ti$^{4+}$ ion (0.26 Å for Si$^{4+}$ and 0.42 Å for Ti$^{4+}$ when the coordination number is 4) [27]. This suggests that Si$^{4+}$ ions substituting for Ti$^{4+}$ ions may have an "off-center" equilibrium position in TiO$_2$. Since there are two participating silicon ions in the defect, it is tempting to consider a model that symmetrically places the two ions at adjacent regular titanium sites oriented along the [001] direction. The two silicon ions would shift slightly toward each other. This model, however, does not account for the observed unequal $^{29}$Si hyperfine interactions and, more importantly, it does not account for the large magnitudes of the two equal $^{47,49}$Ti hyperfine interactions (see Fig. 2). The nearest titanium ions would not be immediately adjacent to the unpaired spin on the two silicon ions, and thus this model predicts only very small splittings for any associated $^{47,49}$Ti interactions.

Because of the small size of the silicon ions, it is more likely that one of the two silicon ions in the present defect substitutes for a titanium ion and the other occupies an adjacent interstitial position. An interstitial silicon is the most obvious way to have two adjacent silicon ions and still have two significant titanium hyperfine interactions. There are two possible interstitial positions in rutile TiO$_2$. One is tetrahedrally coordinated (with four oxygen neighbors), and one is octahedrally coordinated (with six oxygen neighbors). Figure 7(a) identifies the tetrahedral interstitial position with three titanium (Ti$_1$, Ti$_2$, Ti$_3$) and four oxygen (O$_1$, O$_2$, O$_3$, O$_4$) neighbors.

The model illustrated in Fig. 7(b) is proposed for the trapped-hole EPR spectrum reported in the present paper. The paramagnetic charge state of the defect is labeled the [Si$_{int}$ − Si$_{Ti}$]$^+$ center, and the nonparamagnetic state, without the trapped hole, is referred to as the [Si$_{int}$ − Si$_{Ti}$]$^0$ center. The model in Fig. 7(b) satisfies all experimental constraints. One silicon ion (Si$_{Ti}$) replaces the Ti$_1$ ion, and the other silicon ion (Si$_{int}$) occupies the tetrahedral interstitial position. The unpaired spin is shared by these two close silicon ions with the larger portion on the interstitial silicon ion. This model
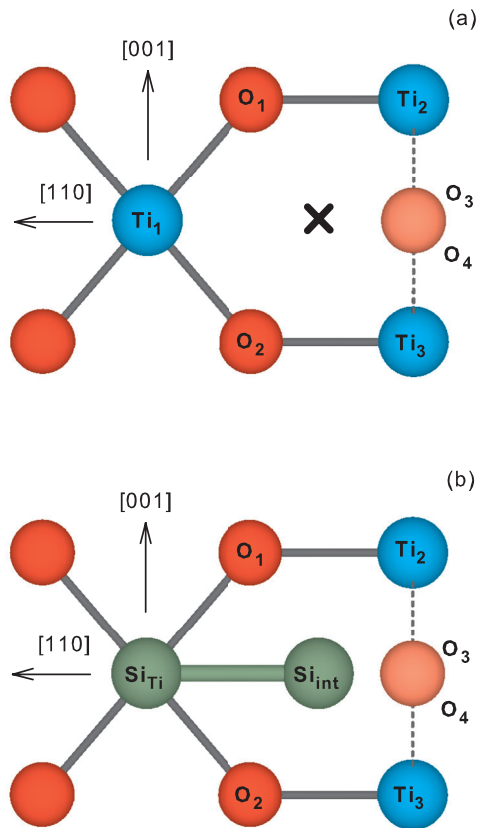
FIG. 7. (Color online) (a) A projection on the $[1\bar{1}0]$ plane of the regular $TiO_2$ crystal. Oxygen ions are red, and titanium ions are blue. The oxygen ion labeled $O_3$ is in front of the plane, and the oxygen ion labeled $O_4$ is behind the plane. A bold **x** marks the tetrahedral interstitial position along the [110] direction. (b) Model of the $[Si_{int} - Si_{Ti}]^+$ defect.

also provides for significant overlap of the unpaired spin onto the two equivalent titanium ions $Ti_2$ and $Ti_3$ next to the silicon interstitial, in agreement with experiment. The two silicon ions form a bond oriented along the [110] direction, which agrees with the directions of the principal axes associated with the unique principal values of the $g$ matrix and $^{29}Si$ hyperfine matrices. If the silicon ion was located at an octahedrally coordinated interstitial position, this Si-Si bond would be along a [100] direction and would disagree with experiment. The observed significant negative $g$ shifts are also explained by the model in Fig. 7(b). All four of the primary ions ($Si_{Ti}$, $Si_{int}$, $Ti_2$, and $Ti_3$) share the unpaired spin, and their relative spin-orbit

interactions are collectively responsible for the magnitudes of the $g$ shifts. The spin-orbit coupling parameter is smaller for silicon compared to titanium [28–31], and thus the titanium ions will make the dominant contributions to these $g$ shifts. This explains why the principal $g$ values for the $[Si_{int} - Si_{Ti}]^+$ center are similar to those previously reported for the family of $Ti^{3+}$ ions in rutile $TiO_2$ crystals [11–14].

An interesting feature of the model in Fig. 7(b) is the arrangement of the four nearest-neighbor oxygen ions around the tetrahedral interstitial position. If a silicon ion is placed at this interstitial site, the four oxygen ions are each separated from the silicon by about 1.7 Å and form an approximate tetrahedron with the silicon at the center. In other words, the silicon and its four oxygen neighbors form a $SiO_4$ unit that is very similar to the highly stable $SiO_4$ units found in many silicates. For comparison, the average Si-O bond distance in $\alpha$-quartz is 1.6 Å [32].

A final structural observation is related to the separation distance between the two silicon ions. In the absence of relaxation, the model in Fig. 7(b) predicts a Si-Si bond length of 2.1 Å. This value is close to the typical bond length of 2.2 Å for doubly bonded disilene compounds [33,34].

## V. SUMMARY

A new and important hole trap has been observed in rutile $TiO_2$ crystals. The responsible defect consists of a closely bound pair of silicon ions, one ion substituting for a titanium and the other at an adjacent tetrahedral interstitial position. These two silicon ions are aligned along the [110] direction. The defect is unique because it represents a hole trap that is independent of the oxygen sublattice. This unexpected behavior primarily arises because one of its components is an interstitial cation. Before trapping a hole, the defect is neutral with no unpaired spins and is labeled the $[Si_{int} - Si_{Ti}]^0$ center. After trapping a hole, the defect is paramagnetic and is referred to as the $[Si_{int} - Si_{Ti}]^+$ center. In this latter charge state, the defect has $S = 1/2$, and its EPR spectrum shows well-resolved hyperfine interactions with two inequivalent $^{29}Si$ nuclei. There are also two equivalent $^{47,49}Ti$ hyperfine interactions because of overlap of the unpaired spin onto two regular titanium ions that are adjacent to the interstitial silicon ion.

[1] A. Fujishima, X. Zhang, and D. A. Tryk, Surf. Sci. Rep. **63**, 515 (2008).

[2] M. A. Henderson, Surf. Sci. Rep. **66**, 185 (2011).

[3] S. Livraghi, M. Rolando, S. Maurelli, M. Chiesa, M. C. Paganini, and E. Giamello, J. Phys. Chem. C **118**, 22141 (2014).

[4] A. Janotti, C. Franchini, J. B. Varley, G. Kresse, and C. G. Van de Walle, Phys. Status Solidi RRL **7**, 199 (2013).

[5] M. Chiesa, M. C. Paganini, S. Livraghi, and E. Giamello, Phys. Chem. Chem. Phys. **15**, 9435 (2013).

[6] S. Livraghi, M. Chiesa, M. C. Paganini, and E. Giamello, J. Phys. Chem. C **115**, 25413 (2011).

[7] S. Livraghi, S. Maurelli, M. C. Paganini, M. Chiesa, and E. Giamello, Angew. Chem. Int. Ed. **50**, 8038 (2011).

[8] A. M. Czoska, S. Livraghi, M. Chiesa, E. Giamello, S. Agnoli, G. Granozzi, E. Finazzi, C. Di Valentin, and G. Pacchioni, J. Phys. Chem. C **112**, 8951 (2008).

[9] C. Di Valentin, G. Pacchioni, and A. Selloni, J. Phys. Chem. C **113**, 20543 (2009).

[10] S. Yang, L. E. Halliburton, A. Manivannan, P. H. Bunton, D. B. Baker, M. Klemm, S. Horn, and A. Fujishima, Appl. Phys. Lett. **94**, 162114 (2009).

[11] S. Yang and L. E. Halliburton, Phys. Rev. B **81**, 035204 (2010).

[12] A. T. Brant, S. Yang, N. C. Giles, and L. E. Halliburton, J. Appl. Phys. **110**, 053714 (2011).

[13] A. T. Brant, N. C. Giles, and L. E. Halliburton, J. Appl. Phys. **113**, 053712 (2013).

[14] S. Yang, A. T. Brant, N. C. Giles, and L. E. Halliburton, Phys. Rev. B **87**, 125201 (2013).

[15] A. T. Brant, N. C. Giles, S. Yang, M. A. R. Sarker, S. Watauchi, M. Nagao, I. Tanaka, D. A. Tryk, A. Manivannan, and L. E. Halliburton, J. Appl. Phys. **114**, 113702 (2013).

[16] A. T. Brant, E. M. Golden, N. C. Giles, S. Yang, M. A. R. Sarker, S. Watauchi, M. Nagao, I. Tanaka, D. A. Tryk, A. Manivannan, and L. E. Halliburton, Phys. Rev. B **89**, 115206 (2014).

[17] S. Yang, A. T. Brant, and L. E. Halliburton, Phys. Rev. B **82**, 035209 (2010).

[18] C. Di Valentin, E. Finazzi, G. Pacchioni, A. Selloni, S. Livraghi, M. C. Paganini, and E. Giamello, Chem. Phys. **339**, 44 (2007).

[19] C. Di Valentin and G. Pacchioni, Acc. Chem. Res. **47**, 3233 (2014).

[20] B. J. Morgan and G. W. Watson, Phys. Rev. B **80**, 233102 (2009).

[21] T. S. Bjørheim, A. Kuwabara, and T. Norby, J. Phys. Chem. C **117**, 5919 (2013).

[22] S. C. Abrahams and J. L. Bernstein, J. Chem. Phys. **55**, 3206 (1971).

[23] C. J. Howard, T. M. Sabine, and F. Dickson, Acta Crystallogr., Sect. B: Struct. Sci. **47**, 462 (1991).

[24] H. J. Gerritsen and H. R. Lewis, Phys. Rev. **119**, 1010 (1960).

[25] T. Purcell and R. A. Weeks, J. Chem. Phys. **54**, 2800 (1971).

[26] J. Kerssen and J. Volger, Physica (Amsterdam) **69**, 535 (1973).

[27] R. D. Shannon, Acta Crystallogr., Sect. A: Cryst. Phys., Diffr., Theor. Gen. Crystallogr. **32**, 751 (1976).

[28] T. M. Dunn, Trans. Faraday Soc. **57**, 1441 (1961).

[29] M. G. Jani, R. B. Bossoli, and L. E. Halliburton, Phys. Rev. B **27**, 2285 (1983).

[30] C. J. Pickard and F. Mauri, Phys. Rev. Lett. **88**, 086403 (2002).

[31] S. Agnello, G. Buscarino, F. M. Gelardi, and R. Boscaino, Phys. Rev. B **77**, 195206 (2008).

[32] Y. Le Page and G. Donnay, Acta Crystallogr., Sect. B: Struct. Crystallogr. Cryst. Chem. **32**, 2456 (1976).

[33] M. Kira and T. Iwamoto, Adv. Organomet. Chem. **54**, 73 (2006).

[34] S. Kyushin, H. Sakurai, T. Betsuyaku, and H. Matsumoto, Organometallics **16**, 5386 (1997).